A parametric vocal fold model based on magnetic resonance imaging

Liang Wu[a)] and Zhaoyan Zhang[b)]
*Department of Head and Neck Surgery, University of California, Los Angeles, 31-24
Rehabilitation Center, 1000 Veteran Avenue, Los Angeles, California 90095-1794, USA
liangwu@xjtu.edu.cn, zyzhang@ucla.edu*

Abstract: This paper introduces a parametric three-dimensional body-cover vocal fold model based on magnetic resonance imaging (MRI) of the human larynx. Major geometric features that are observed in the MRI images but missing in current vocal fold models are discussed, and their influence on vocal fold vibration is evaluated using eigenmode analysis. Proper boundary conditions for the model are also discussed. Based on control parameters corresponding to anatomic landmarks that can be easily measured, this model can be adapted toward a subject-specific vocal fold model for voice production research and clinical applications.
© 2016 Acoustical Society of America
[AL]

1. Introduction

Continuum models of phonation allow systematic investigation of the physics of voice production and control, which is often difficult in *in vivo* experiments. Due to the complex physics involved, simplified vocal fold geometry is often used in current continuum models of phonation. One of the first continuum models of the vocal fold (Titze and Strong, 1975) used a rectangular prism to model the vocal fold. Anterior–posterior and superior–inferior variations in vocal fold depth (dimension along the medial-lateral direction) were incorporated in later models (e.g., Titze and Talkin, 1979; Alipour *et al.*, 2000). Although such simplifications are necessary in order to focus on the basic physical mechanisms of phonation, recent studies (Pickup and Thomson, 2010, 2011; Zhang, 2016) have shown that vocal fold geometry has important influence on the resulting vocal fold vibration and voice production. Thus, there is an increasing need to develop continuum models with more realistic vocal fold geometry. Clinically, continuum models based on realistic geometry may lead to the development of subject-specific tools that help predict and optimize voice outcomes of clinical intervention of voice disorders.

In this study, a parametric three-dimensional (3D) vocal fold model is developed, with geometry obtained from magnetic resonance imaging (MRI). Although there are some previous MRI studies of vocal fold geometry (Storck *et al.*, 2012; Klepacek *et al.*, 2015), the goal of this study is to derive a mathematic model of vocal fold geometry that allows subject-specific adaption and can be easily reproduced by other research groups. Additionally, major features of this MRI-based model that are missing in current vocal fold models are discussed, and their relevance to vocal fold vibration is evaluated by eigenmode analysis.

2. Methods

Two cadaver hemi-larynges (S1 and S2) from two men (28 and 22 yrs old) were used for MRI scanning. Each sample was frozen at -80 °C after dissection and thawed on the day of experiment. The sample was supported by foam (Mr. Clean, Cincinnati, OH) and placed inside a plastic 5-cm diameter cylindrical container, which was filled with Fomblin oil (Kurt J. Lesker Company, Livermore, CA) in order to reduce tissue dehydration and possible imaging distortions due to air-tissue interface during the scan. Both samples were scanned by a Bruker BioSpec 7 Tesla MRI (Bruker Biospin GmbH, Rheinstetten, Germany) with a receive-only surface coil (30-mm inner diameter). A standard rapid acquisition with relaxation enhancement imaging sequence was applied to obtain a high quality image using the following settings: a repetition time of

---

[a)]Present address: Department of Biomedical Engineering, School of Life Science and Technology, Xi'an
Jiaotong University, Xi'an 710049, People's Republic of China.
[b)]Author to whom correspondence should be addressed.

3500 ms, an echo time of 43 ms (S1) and 39 ms (S2), a turbo factor of 12, and a field of view of $4.2 \times 4.0 \times 2.5 \, cm^3$ (S1) and $4.0 \times 3.5 \times 1.8 \, cm^3$ (S2) with a spatial resolution of $100 \times 100 \times 100 \, \mu m^3$. The scan time was 8 h 30 m for S1 and 5 h 46 m for S2.

The MRI images were processed using Mimics software (The Materialise Group, Leuven, Belgium). The cartilages (including the thyroid, cricoid, and arytenoid cartilages), laryngeal muscles [including the thyroarytenoid (TA) muscle, lateral cricoarytenoid (LCA) muscle, interarytenoid (IA) muscle, and cricothyroid muscle], and cover layer (the lamina propria and epithelium) were segmented using manual tools provided in the software. Finally, a 3D vocal fold model was reconstructed from the segmentations using Gaussian smoothing.

3. 3D human vocal fold structure

Figure 1 shows the original MRI images with the segmented cartilages, muscles, and tissue layers obtained using larynx S1. Some important geometric features of the TA muscle and the cover layer, which includes the lamina propria and epithelium, can be noted. First, in the axial plane, the TA muscle has a large depth in the middle and the depth decreases toward the anterior and posterior ends. The TA muscle and the thyroid cartilage are not in direct contact in the inferior and posterior portions, separated by the LCA muscle. This is different from current computational vocal fold models, in which the entire lateral surface of the vocal fold is often assumed to attach to the thyroid cartilage and a fixed boundary condition is often imposed. Second, in the coronal plane, the TA muscle has a triangular shape with curved edges. Third, in the sagittal view, the TA muscle thickness decreases continuously from the anterior to the posterior end. This thickness variation is more significant in sample S2 as shown in Fig. 1. Finally, the TA has a considerable posterior volume lateral to the arytenoid cartilage. Except for the second feature, the other features are generally not included in current computational vocal fold models.

The cover layer is outlined in light pink in Fig. 1. From the axial and sagittal views, the thickness of the cover layer is relatively uniform along the anterior–posterior direction. In the coronal plane, the cover layer thickness increases slightly toward the inferior end.

4. Parametric vocal fold model

4.1 Model description

A parametric vocal fold model is developed based on the MRI images. The model includes a body layer (the TA muscle) and a cover layer. The body layer was reconstructed from three anchor curves that define the lateral-superior (C_A), medial (C_B), and inferior (C_C) outer contour of the TA muscle, as shown in Fig. 1. These three curves are again defined based on eight control points (P_{A1}, P_{A2}, P_{B1}, P_{B2}, P_{C1}, P_{C2}, P_{C3}, P_{C4}; Fig. 2), whose coordinates can be directly measured from MRI images or anatomical landmarks of the TA muscle. For example, points P_{A1} and P_{A2} are the points that are farthest from the medial edge C_B in the lateral and superior direction, respectively. Note that, for convenience, the anterior medial edge of the TA muscle is set at the origin in Fig. 2, and the control point P_{B1} corresponds to the location of the vocal process. Based on the coordinates of the eight control points, the three anchor

1 – Thyroid Cartilage; 2 – Arytenoid Cartilage;
3 – Cricoid Cartilage; 4 – Thyroarytenoid (TA) muscle;
5 – Cover layer (lamina propria & epithelium);
6 – Lateral cricoarytenoid (LCA) muscle;
7 – Cricothyroid (CT) muscle;
8 – Posterior cricoarytenoid (PCA) muscle;
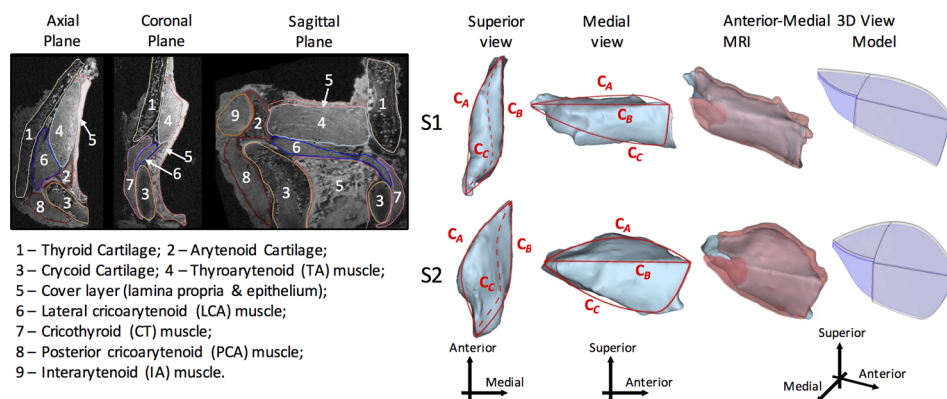9 – Interarytenoid (IA) muscle.

Fig. 1. (Color online) The original segmented MRI images for S1 (left) and the 3D reconstruction of the two larynges (TA and cover) and the corresponding vocal fold models (right). The MRI images outline the cartilages, muscles, and cover layer (lamina propria and epithelium). The 3D reconstruction images show the TA muscle (light blue) and cover layer (light pink). The curves represent the three anchor curves of the TA muscle (see Fig. 2).
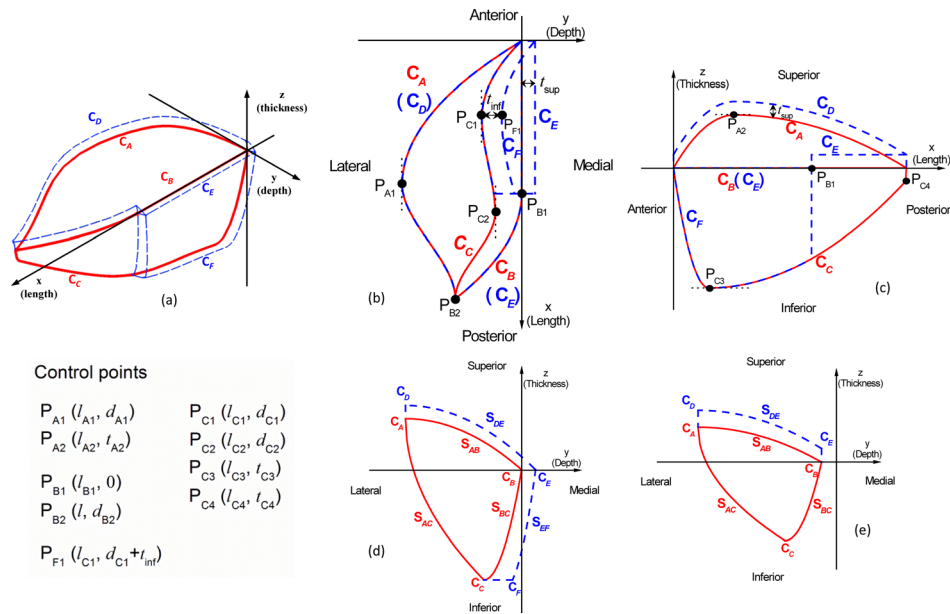
Fig. 2. (Color online) Geometry description of the parametric vocal fold model in a 3D view (a), from a superior view (b), a lateral view (c), and coronal plane at an anterior (d) and posterior section (e). The solid curves represent the anchor curves of the TA muscle, and the dashed curves are the anchor curves of the cover layer. The black solid circles refer to the control points which determine the curves. Points, curves, and surfaces are denoted with an initial letter of P, C, and S, respectively. For the coordinates of the control points, the initial letter l means length in the anterior-posterior (x) direction, d for the depth in the medial-lateral (y) direction, and t for thickness in the superior-inferior (z) direction.

curves are described by piecewise quadratic or cubic polynomial functions (see the Appendix). The continuity of the piecewise function guaranteed the smoothness of the curve at the control points. Based on these three anchor curves, three curved surfaces of the TA muscle can be formed, with the mathematic equations describing these surfaces listed in the Appendix. The reconstructed 3D model of the TA muscle is shown in Figs. 1 and 2.

Similar to the TA muscle, the superior and medial surfaces of the cover layer are determined by three anchor curves, which are the lateral-superior (C_D), medial (C_E), and inferior (C_F) edges. The inner surfaces of the cover layer are in contact with the superior and medial surfaces of the TA muscle. curve C_D is related to curve C_A by an upward shift of t_{sup} that corresponds to the cover layer thickness in the z direction, whereas curve C_E is related to curve C_B by a medial shift of t_{sup} in the y direction. Curve C_F is defined with an additional control point P_{F1}, which is obtained by moving the control point P_{C1} medially by a distance of t_{inf} [Fig. 2(b)]. The MRI images show that the cover layer extends as long as the TA muscle in the anterior-posterior direction (Fig. 1). However, because the posterior portion of the cover layer is fixed to the arytenoid cartilage and often becomes stiffer toward the vocal process, the portion of
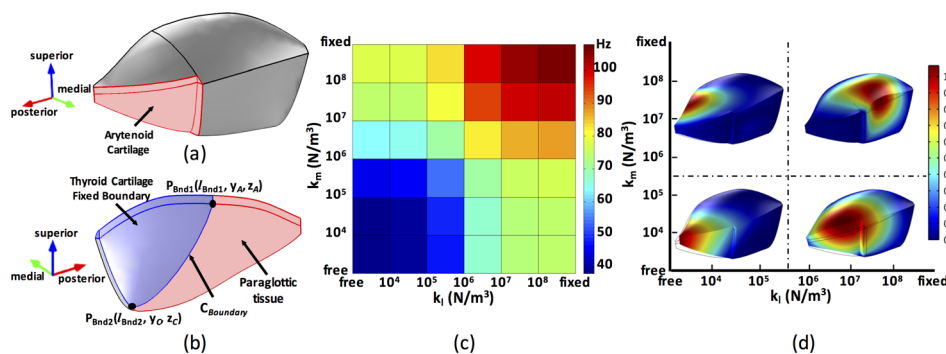

Fig. 3. (Color online) Posterior-medial view (a) and anterior-lateral view (b) of the vocal fold model illustrating different boundary conditions. The curve $C_{Boundary}$ in (b) is determined by the two control points P_{Bnd1} and P_{Bnd2}. (c) and (d) show the first *in vacuo* eigenfrequency and its typical vibration pattern as a function of the lateral and medial spring foundation constants k_l and k_m applied to the posterior-lateral and posterior-medial surfaces, respectively.

Table 1. Model parameters extracted from the MRI images. (Unit: mm.)

	P_{A1}		P_{A2}		P_{B1}	P_{B2}		P_{C1}		P_{C2}		P_{C3}		P_{C4}	Cover layer		$C_{Boundary}$	
	l_{A1}	d_{A1}	l_{A2}	t_{A2}	l_{B1}	l	d_{B2}	l_{C1}	d_{C1}	l_{C2}	d_{C2}	l_{C3}	t_{C3}	t_{C4}	t_{sup}	t_{inf}	l_{Bnd1}	l_{Bnd2}
S1	15.3	−7.2	6.9	2.1	16.7	27.1	−8.0	8.2	−3.2	19.8	−2.2	1.1	−9.1	−0.7	0.6	1.1	11.4	3.2
S2	15.0	−8.9	7.2	4.1	16.1	27.2	−5.2	8.3	−3.1	17.9	−2.2	4.4	−8.7	−0.9	0.7	1.3	14.6	5.4

the cover layer that is posterior to the vocal process (control point P_{B1}) is excluded from the model. With the determination of C_D, C_E, and C_F, the two outer surfaces of the cover layer S_{DE} and S_{EF} can be formed according to equations in the Appendix [Fig. 1 and Figs. 2(d) and 2(e)].

An additional curve $C_{Boundary}$ is added on the lateral surface of the body layer to define the boundary of the region on the lateral surface that is in contact with the thyroid cartilage [Fig. 3(b)]. This curve is defined based on two additional control points P_{Bnd1} and P_{Bnd2} [Fig. 3(b); Appendix].

4.2 Boundary condition

The superior surface and anterior-medial surface are fluid-structure interaction surfaces. The anterior lateral surface is attached to the thyroid cartilage and thus should be set as a fixed boundary. The posterior-lateral surface [pink in Fig. 3(b)] is in contact with the paraglottic tissue layer which includes the LCA muscle and some fat tissues. Thus, this surface has some degree of freedom to move and a fixed boundary condition would prevent vocal fold adduction and is not appropriate. In previous studies an impedance boundary condition is often used by attaching this surface to a spring foundation (Yin and Zhang, 2014) or an adipose layer (Jones *et al.*, 2015). Similarly, the posterior-medial surface is attached to the arytenoid cartilage, and a fixed boundary condition may not be appropriate in voicing conditions when the arytenoid cartilage is not completely constrained and has some freedom to move. All the rest of the surfaces are fixed boundaries.

4.3 Validation and general model behaviors

Table 1 lists all the model parameters, which correspond to the coordinates of the control points, for the two larynges. Figure 1 compares the computational vocal fold model derived based on values in Table 1 to the original MRI-reconstructed 3D vocal fold structure for the two larynges. In general, a reasonably good match between the model and the MRI geometries is obtained. To evaluate the vibrational similarity between the model and the MRI geometry, Table 2 compares the first five *in vacuo* eigenfrequencies of the model and MRI geometry for larynx S2, calculated using the commercial software COMSOL and imposing a fixed boundary condition to both the posterior-lateral and posterior-medial surfaces. Table 2 shows a maximum relative difference of 4.3% in eigenfrequencies between the vocal fold model and the original MRI geometry, indicating that the model captures most of the geometric features of vibrational consequence. A similarly small difference is obtained for S1.

In current vocal fold models, the posterior part of the vocal fold that is lateral to the arytenoid cartilage is often excluded. To evaluate the importance of this posterior component, Table 2 also shows the eigenfrequencies of the vocal fold model when this part is removed. Removing this part significantly increases the eigenfrequencies, indicating the importance to including it in vocal fold models.

To evaluate the effect of the boundary conditions on the posterior-lateral and posterior-medial surfaces, Fig. 3(c) shows the first eigenfrequency of the vocal fold model for S2, with the posterior-lateral and posterior-medial surfaces attached to a

Table 2. First five *in vacuo* eigenfrequencies of the model and the MRI geometry for the sample S2. (Unit: Hz.)

Modes	TA		TA and cover layer		TA and cover layer Model without posterior part
	MRI	Model	MRI	Model	
1	79.94	78.09	75.06	75.20	115.83
2	110.14	114.06	102.70	107.14	135.81
3	116.94	119.86	112.76	115.21	153.28
4	129.09	130.03	126.71	122.20	166.10
5	141.82	147.98	136.81	139.31	184.96

spring foundation with a spring constant of k_l and k_m, respectively. As expected, increasing either spring constant increases the eigenfrequency. The values of the spring constants also have a significant influence on the vibration pattern of the eigenmodes. Figure 3(d) shows a typical vibration pattern of the first *in vacuo* mode in the four quadrants. For small lateral spring constants, large vocal fold vibration is limited to the lateral and posterior parts of the vocal folds, with almost no motion along the medial surface. Similarly, small medial spring constants lead to dominant motion along the posterior-medial portion of the vocal fold that is close to the arytenoid cartilage. Thus, in order to achieve large vocal fold motion along the medial surface, both the posterior-lateral and posterior-medial surfaces need to be constrained to some degree, presumably through LCA/TA activation for the posterior-lateral surface and LCA/IA/TA activation (probably also the posterior cricoarytenoid muscle) for the posterior-medial surface. These adjustments however do provide an additional approach to control fundamental frequency and vocal fold vibration pattern that is not included in current vocal fold models.

5. Conclusion

A mathematic model of the 3D vocal fold geometry is developed based on MRI images. Proper boundary conditions for the newly-developed model are also discussed. This model can be easily adapted to individual anatomic dimensions toward the development of a subject-specific phonation model. Parametric studies of voice production using this model would also allow better understanding of voice production and control in realistic human conditions, which will be the focus of our future work.

Acknowledgments

Appendix: Mathematical equations of the vocal fold model

(1) Equations for the anchor curves of TA muscle and cover layer.
Curve C_A:

$$x_A \in [0, l], \quad y_A = \begin{cases} a_{11}x^2 + b_{11}x, & x \in [0, l_{A1}] \\ a_{12}(x - l_{A1})^3 + b_{12}(x - l_{A1})^2 + d_{12}, & x \in [l_{A1}, l]; \end{cases}$$

$$z_A = \begin{cases} a_{13}x^2 + b_{13}x, & x \in [0, l_{A2}] \\ a_{14}(x - l_{A2})^2 + c_{14}, & x \in [l_{A2}, l], \end{cases}$$

where

$$a_{11} = \frac{-d_{A1}}{l_{A1}^2}; \quad b_{11} = \frac{2d_{A1}}{l_{A1}}; \quad a_{12} = \frac{-2(d_{B2} - d_{A1})}{(l - l_{A1})^3}; \quad b_{12} = \frac{3(d_{B2} - d_{A1})}{(l - l_{A1})^2};$$

$$d_{12} = d_{A1}; \quad a_{13} = \frac{-t_{A2}}{l_{A2}^2}; \quad b_{13} = \frac{2t_{A2}}{l_{A2}}; \quad a_{14} = \frac{-t_{A2}}{(l - l_{A2})^2}; \quad c_{14} = t_{A2}.$$

Curve C_B:

$$x_B \in [0, l], \quad z_B = 0, \quad y_B = \begin{cases} 0, & x \in [0, l_{B1}] \\ a_{21}(x - l_{B1})^2, & x \in [l_{B1}, l] \end{cases}, \quad \text{where } a_{21} = \frac{d_{B2}}{(l - l_{B1})^2}.$$

Curve C_C:

$$x_C \in [0, l], \quad y_C = \begin{cases} a_{31}x^2 + b_{31}x, & x \in [0, l_{C1}] \\ a_{32}(x - l_{C1})^3 + b_{32}(x - l_{C1})^2 + d_{32}, & x \in [l_{C1}, l_{C2}] \\ a_{33}(x - l_{C2})^3 + b_{33}(x - l_{C2})^2 + d_{33}, & x \in [l_{C2}, l]; \end{cases}$$

$$z_C = \begin{cases} a_{34}x^2 + b_{34}x, & x \in [0, l_{C3}] \\ a_{35}(x - l_{C3})^2 + c_{35}, & x \in [l_{C3}, l], \end{cases}$$

where

$$a_{31} = \frac{-d_{C1}}{l_{C1}^2}; \quad b_{31} = \frac{2d_{C1}}{l_{C1}}; \quad a_{32} = \frac{-2(d_{C2} - d_{C1})}{(l_{C2} - l_{C1})^3}; \quad b_{32} = \frac{3(d_{C2} - d_{C1})}{(l_{C2} - l_{C1})^2};$$

$$d_{32} = d_{C1}; \quad a_{33} = \frac{-2(d_{B2} - d_{C2})}{(l - l_{C2})^3}; \quad b_{33} = \frac{3(d_{B2} - d_{C2})}{(l - l_{C2})^2}; \quad d_{33} = d_{C2};$$

$$a_{34} = \frac{-t_{C3}}{l_{C3}^2}; \quad b_{34} = \frac{2t_{C3}}{l_{C3}}; \quad a_{35} = \frac{t_{C4} - t_{C3}}{(l - l_{C3})^2}; \quad c_{35} = t_{C3}.$$

Curve C_D:

$$x_D \in [0, l], \quad y_D = y_A, \quad z_D = z_A + t_{\text{sup}}.$$

Curve C_E:

$$x_E \in [0, l], \quad y_E = \begin{cases} t_{\text{sup}}, & x \in [0, l_{B1}] \\ y_B, & x \in [l_{B1}, l], \end{cases}$$

$$z_E = \begin{cases} 0, & x \in [0, l_{B1}] \\ z_D(l_{B1}) \cdot \left[1 - \left(\frac{y_D(l_{B1})}{t_{\text{sup}} - y_D(l_{B1})} \right)^2 \right], & x \in [l_{B1}, l]. \end{cases}$$

Curve C_F:

$$x_F \in [0, l_{B1}], \quad z_F = z_C, \quad y_F = \begin{cases} a_{41}x^2 + b_{41}x + c_{41}, & x \in [0, l_{C1}] \\ a_{42}(x - l_{C1})^3 + b_{42}(x - l_{C1})^2 + d_{42}, & x \in [l_{C1}, l_{B1}], \end{cases}$$

where

$$a_{41} = \frac{-(d_{C1} + t_{\text{inf}} - t_{\text{sup}})}{l_{C1}^2}; \quad b_{41} = \frac{2(d_{C1} + t_{\text{inf}} - t_{\text{sup}})}{l_{C1}};$$

$$c_{41} = t_{\text{sup}}; \quad a_{42} = \frac{-2(t_{\text{sup}} - d_{C1} - t_{\text{inf}})}{(l - l_{C1})^3}; \quad b_{42} = \frac{3(t_{\text{sup}} - d_{C1} - t_{\text{inf}})}{(l - l_{C1})^2}; \quad d_{42} = d_{C1} + t_{\text{inf}}.$$

Curve C_{Boundary}:

$$x_{Bnd} \in [l_{\text{Bnd2}}, l_{\text{Bnd1}}].$$

$$z_{\text{Bnd}} = a_{\text{Bnd}}(x - l_{\text{Bnd2}})^2 + c_{\text{Bnd}}; \quad y_{\text{Bnd}} = y_A(x) + (y_C(x) - y_A(x)) * \left(\frac{z_{\text{Bnd}}(x) - z_A(x)}{z_C(x) - z_A(x)} \right)^2,$$

where

$$a_{\text{Bnd}} = \frac{z_A(l_{\text{Bnd1}}) - z_C(l_{\text{Bnd2}})}{(l_{\text{Bnd1}} - l_{\text{Bnd2}})^2}; \quad c_{\text{Bnd}} = z_C(l_{\text{Bnd2}}).$$

(2) Equations for the curved surfaces.

Surface S_{AB}:

$$x_{AB} \in [0, l], \quad y_{AB} \in [y_A(x), y_B(x)], \quad z_{AB} = a_{51}(y - y_B(x))^2 + b_{51}(y - y_B(x)),$$

where

$$a_{51} = \frac{-z_A(x)}{(y_A(x) - y_B(x))^2}; \quad b_{51} = \frac{2z_A(x)}{y_A(x) - y_B(x)}.$$

Surface S_{BC}:

$$x_{BC} \in [0, l], \quad y_{BC} \in [y_C(x), y_B(x)], \quad z_{BC} = a_{61}(y - y_C(x))^2 + c_{61}, \text{ where}$$

$$a_{61} = \frac{-z_C(x)}{(y_B(x) - y_C(x))^2}; \quad c_{61} = z_c(x).$$

Surface S_{AC}:

$$x_{AC} \in [0, l], \quad y_{AC} \in [y_A(x), y_C(x)], \quad z_{AC} = a_{71}\sqrt{y - y_A(x)} + c_{71}, \text{ where}$$

$$a_{71} = \frac{z_C(x) - z_A(x)}{\sqrt{y_C(x) - y_A(x)}}; \quad c_{71} = z_A(x).$$

Surface S_{DE}:

$$x_{DE} \in [0, l], \quad y_{DE} \in [y_D(x), y_E(x)], \quad z_{DE} = a_{81}(y - y_E(x))^2 + b_{81}(y - y_E(x)) + c_{81},$$

where

$$a_{81} = \frac{-(z_D(x) - z_E(x))}{(y_D(x) - y_E(x))^2}; \quad b_{81} = \frac{2(z_D(x) - z_E(x))}{y_D(x) - y_E(x)}; \quad c_{81} = z_E(x).$$

Surface S_{EF}:

$$x_{EF} \in [0, l_{B1}], \; y_{EF} \in [y_F(x), y_E(x)], \; z_{EF} = a_{91}(y - y_F(x))^2 + c_{91},$$

$$\text{where} \quad a_{91} = \frac{-z_F(x)}{(y_E(x) - y_F(x))^2}; \quad c_{91} = z_F(x).$$

References and links

Alipour, F., Berry, D. A., and Titze, I. R. (**2000**). "A finite-element model of vocal-fold vibration," J. Acoust. Soc. Am. **108**, 3003–3012.

Jones, C. L., Achuthan, A., and Erath, B. D. (**2015**). "Modal response of a computational vocal fold model with a substrate layer of adipose tissue," J. Acoust. Soc. Am. **137**, EL158–EL164.

Klepacek, I., Jirak, D., Smrckova, M. D., Janouskova, O., and Vampola, T. (**2015**). "The human vocal fold layers. Their delineation inside vocal fold as a background to create 3D digital and synthetic glottal model," J. Voice, available online, doi:10.1016/j.jvoice.2015.08.004

Pickup, B. A., and Thomson, S. L. (**2010**). "Flow-induced vibratory response of idealized versus magnetic resonance imaging-based synthetic vocal fold models," J. Acoust. Soc. Am. **128**, EL124–EL129.

Pickup, B. A., and Thomson, S. L. (**2011**). "Identification of geometric parameters influencing the flow-induced vibration of a two-layer self-oscillating computational vocal fold model," J. Acoust. Soc. Am. **129**, 2121–2132.

Storck, C., Gehrer, R., Hofer, M., Neumayer, B., Stollberger, R., Schumacher, R., Gugatschka, M., Friedrich, G., and Wolfensberger, M. (**2012**). "Laryngeal electromyography: Electrode guidance based on 3-Dimensional magnetic resonance tomography images of the larynx," J. Voice **26**, 110–116.

Titze, I. R., and Strong, W. (**1975**). "Normal modes in vocal cord tissues," J. Acoust. Soc. Am. **57**, 736–744.

Titze, I. R., and Talkin, D. T. (**1979**). "A theoretical study of the effects of various laryngeal configurations on the acoustics of phonation," J. Acoust. Soc. Am. **66**, 60–74.

Yin, J., and Zhang, Z. (**2014**). "Interaction between the thyroarytenoid and lateral cricoarytenoid muscles in the control of vocal fold adduction and eigenfrequencies," J. Biomech. Eng. **136**, 111006.

Zhang, Z. (**2016**). "Cause-effect relationship between vocal fold physiology and voice production in a three-dimensional phonation model," J. Acoust. Soc. Am. **139**, 1493–1507.